Ocean Engineering 274 (2023) 114025

Contents lists available at ScienceDirect

Ocean Engineering

journal homepage: www.elsevier.com/locate/oceaneng

Numerical investigations of a pivoted point absorber wave energy converter integrated with breakwater using CFD

Injun Yang [a,*], Tahsin Tezdogan [b], Atilla Incecik [a]

[a] Department of Naval Architecture, Ocean and Marine Engineering, Henry Dyer Building, University of Strathclyde, 100 Montrose Street, Glasgow, G4 0LZ, UK
[b] Department of Civil, Maritime and Environmental Engineering, University of Southampton, Southampton, UK

ARTICLE INFO

Handling Editor: Prof. A.I. Incecik

Keywords:
Wave energy converter
Fixed breakwater
CFD
Stationary wave
Pivoted point absorber

ABSTRACT

Wave energy resources are enormous and widely distributed worldwide and evaluated as resources to replace fossil fuels. One of the methods to collect wave energy is using a point absorber device, which is a device designed to react sensitively to the movement of the water surface for harnessing wave energy. This paper is about the influence of a fixed breakwater on a Wavestar-shaped pivoted point absorber wave energy converter (WEC) using computational fluid dynamics (CFD). The fixed breakwater may generate a stationary wave and this phenomenon helps to enlarge the movement of the water surface. The numerical model based on CFD was validated against the available published data and verified to prove the accuracy of the numerical solution. It was found that the present numerical results have a good agreement with the available experimental results. A parametric study was conducted to understand the influence of the fixed breakwater on the WEC. The gap between the fixed breakwater and a buoy of the WEC has been changed according to wave period and the results depending on the gap have been compared. The results suggest a better hydrodynamic performance of the motion responses of the WEC, compared to those without the fixed breakwater. A stationary wave equation considering the gap was derived as a trigonometric function in order to investigate the correlation between a stationary wave and the motion response.

1. Introduction

Due to climate change, many researchers are steadily working on ways to reduce greenhouse gases. Since coal, oil, and natural gas for the production of electric energy are still mainstream industries, various energy industries have been proposed to replace them and have reached the commercialisation stage. Among the renewable energy industries, a variety of methods have been proposed in the field using wave energy, and great efforts are being made to develop it into a commercialisation stage.

A wave energy converter (WEC) device is one of the ways to produce electricity from wave energy. The big advantage of the WEC is that it can be installed everywhere the waves are observed, therefore, a high number of types of WEC have been introduced and the development of new WEC concepts is still ongoing to increase the efficiency of energy capture from the waves. There are great efforts to put the developed WEC devices on the commercial stage, for example, Oscillating-Water Column (OWC) plants like Pico (Paparella et al., 2015), the Pelamis (Yemm et al., 2012), overtopping WEC types like the Wave Dragon (Kofoed et al., 2006), the point absorber type for SEAREV (Ruellan et al., 2010) and the Wavestar (Kramer et al., 2011). Deep and detailed information on the WEC according to the working principle of the device and the location installed such as onshore and offshore can be found in (Day et al., 2015; Falcão, 2010; Pecher and Kofoed, 2017). As described above, several efforts have been made to deliver the WEC devices to the commercial stage, but developments were often suspended due to insufficient financial support. In order to proceed to the commercial stage, it is essential to produce a prototype and go through its own verification and supplementation steps. In addition, most prototypes are quite large in size, so costs of construction and maintenance are also significantly high. To this end, support from the government and private enterprise are inevitable. Although many studies regarding to WECs have been conducted, it looks that the more accumulation of technology and development are fundamental to lead to the commercial stage.

Depending on the operating principles of WECs, groups of device types using the terms point absorber (PA), terminator, attenuator, oscillating wave surge converter (OWSC), oscillating water column (OWC), pressure differential, and rotating mass are used by the

* Corresponding author.
E-mail address: injun.yang@strath.ac.uk (I. Yang).

https://doi.org/10.1016/j.oceaneng.2023.114025
Received 4 October 2022; Received in revised form 12 February 2023; Accepted 18 February 2023
Available online 28 February 2023
0029-8018/© 2023 The Authors. Published by Elsevier Ltd. This is an open access article under the CC BY license (http://creativecommons.org/licenses/by/4.0/).

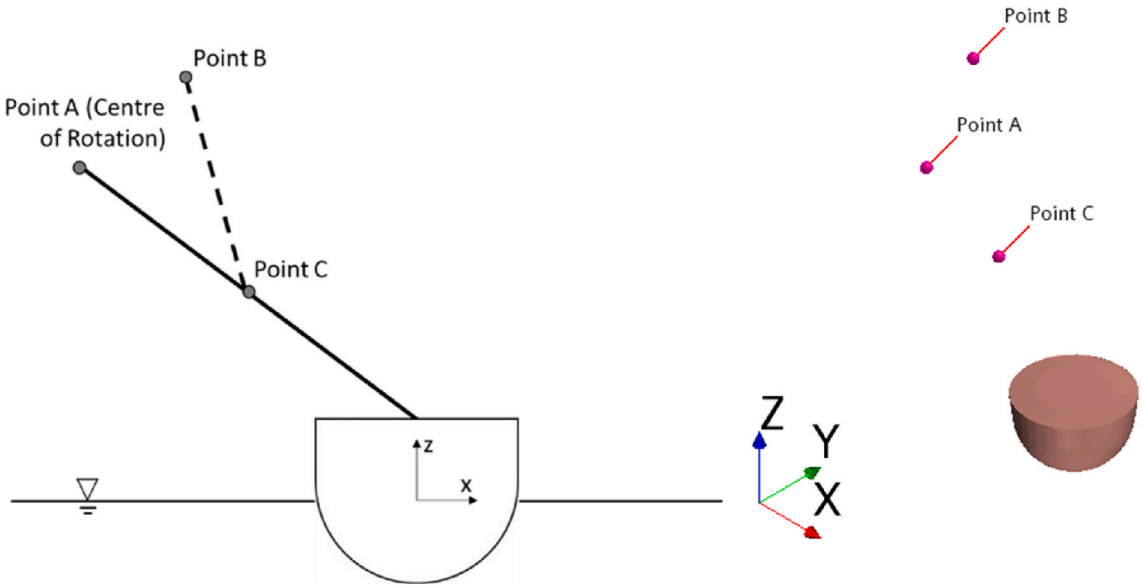

Fig. 1. Schematic of the WEC (not at scale, left) and 3D geometry (right), including the centre of rotation (Point A) and the position of the hydraulic PTO cylinder (Point B and C).

European Marine Energy Centre (EMEC). A PA is consisted of small sized floating structure compared to the wavelength, absorbing energy from all direction. Terminators are installed widely parallel to the incident wave fronts to capture and break as much of the incoming wave as possible. Attenuators are consisted of floating devices which are aligned parallel to the incident wave direction and intercept energy from the relative motion of subsections of WEC as the incident wave passes through the devices. OWSCs use surges of the incident wave to extract energy. OWCs contain a submerged air chamber including an opening in the front skirt and a hole in the top. The water column inside the chamber is forced to oscillate by the incident waves and its movement is captured by a turbine in the top. Pressure differential devices are typically located below sea level and pumps fluid through a system using pressure change caused by waves. Rotating mass devices capture wave energy by the movement of two forms of rotation due to heaving and swaying in the waves.

According to reviews of Mustapa et al. (2017) and Zhao et al. (2019) a,b, the combination of WEC device with other marine facilities such as breakwaters has become common for coastal areas. The benefits of cost-sharing, space-sharing and multi-functionality by the integration of marine structures lead reducing the construction cost. Some innovative research about floating breakwaters combined with WECs, which generates electricity using the heave motion, can be found in those studies; a moonpool type floating breakwater-WEC (Cheng et al., 2021; Tay, 2022a, 2022b), a pontoon type floating breakwater-WEC (Guo et al., 2020; Ning et al., 2017, 2018), a vertical pile-restrained WEC type (Chen et al., 2020; Ning et al., 2016), a Comb-type breakwater-WEC (Zhao et al., 2020, 2021; Zhao et al., 2019a,b) and the Berkeley Wedge (TBW) type (Tom et al., 2018, 2019; Zhang et al., 2019). The main objective of those research studies is to enhance the performance of the WEC and the wave attenuation function of the floating breakwaters. Another approach of the integration of breakwaters and WECs is the combination of WECs and a fixed breakwater. McIver and Evans (1988), Mavrakos et al. (2004), and Schay et al. (2013) found that the power obtained by Pas in front of a fixed breakwater was much greater than that obtained by the same independent Pas. Coiro et al. (2016) mentioned the stationary wave system which was established in front of the breakwater wall itself because of the incident wave and the reflected wave from the wall. They expected that the stationary wave system should be very sensitive to the incident wavelength, which would affect the performance of the power output. Reabroy et al. (2019) studied the differences in the WEC motion with the distance between the WEC and the breakwater wall in a certain wave period and found that the breakwater effect indicated that the point absorber type of WEC can improve the hydrodynamic performance of WEC such as the heave motion of the WEC. However, the range of the distance they conducted to obtain the optimal distance is relatively shorter than the wavelength which is not expected to amplify the motion of the WEC due to the stationary wave. There were many attempts to investigate the integration of fixed breakwater-WEC using a linear potential flow theory (Konispoliatis and Mavrakos (2020), Konispoliatis and Mavrakos (2021) and Zhao et al. (2019)a,b). Those studies include the parametric study of the breakwater-WEC spacing including the gap between WEC devices and the breakwaters and the arrangement study of WECs. Wang et al. (2022) has investigated the hydrodynamic performance of the PA with Jarlan-type breakwater, which is conventional breakwater type in coastal area. The most common consideration regarding to the integration of fixed breakwater-WEC is generally how to adjust the gap between the fixed breakwater and WEC device in order to enhance the wave power absorption.

The numerical studies using computational fluid dynamics (CFD) to understand the characteristics of WEC are gradually increasing. One aim of these numerical studies is to secure numerical tools through the validation of experiments in order to conduct further research. A comprehensive review of the WEC research using CFD over the past two decades can be found in Windt et al. (2018). When CFD is used in WEC's research and development, cost savings can be obtained compared to experiments, and numerical studies can be performed under various environmental and physical conditions without significant restrictions. Therefore, it is considered that the importance of acquiring the numerical tools for WEC using CFD is an increasing trend amongst the researchers working in this area. Most of studies related to the combination of WEC device with marine facilities have been investigated by a linear potential flow theory and experimental method. To date, majority of the CFD studies with WECs have focused on the sole WEC such as their heave response to the incident wave. It is expected that this study's CFD work will help to understand the influence of the gap between a WEC device and a breakwater at intermediate water depth.

Given the importance of the integration of breakwater-WEC, to the best of the authors' knowledge, there exists no CFD study dedicated to the influence of a gap between the fixed breakwater and the WEC. Thus, this paper is motivated to understand the influence of the gap in different wave conditions at intermediate water depth. The outline of

Table 1
Physical properties of the target wave energy converter.

	Unit	Value
Mass	*kg*	220
Centre of Mass:		
X	*m*	−0.2886
Y	*m*	0
Z	*m*	0.3245
Moment of Inertia	kgm^2	124.26
Centre of rotation (Point A)		
X	*m*	−1.684
Y	*m*	0
Z	*m*	1.655
Point B		
X	*m*	−1.147
Y	*m*	0
Z	*m*	3.004
Point C (relative to the centre of mass)		
X	*m*	−0.5684
Y	*m*	0
Z	*m*	0.8635
Submergence (in equilibrium)	*m*	0.4
Diameter of a buoy (at SWL)	*m*	1.0
Water depth	*m*	3.0

Table 2
Wave cases to which the present numerical simulation is applied.

Case number C	Wave period [s] T	Wavelength [m] λ	Wave height [m] H	Wave steepness H/λ
1	1.4	3.06	0.25	0.082
2	1.6	4.00	0.25	0.063
3	1.8	5.06	0.25	0.049
4	2.0	6.25	0.25	0.040
5	2.2	7.56	0.25	0.033
6	2.4	8.99	0.25	0.028
7	2.6	10.55	0.25	0.024
8	2.8	12.24	0.25	0.020

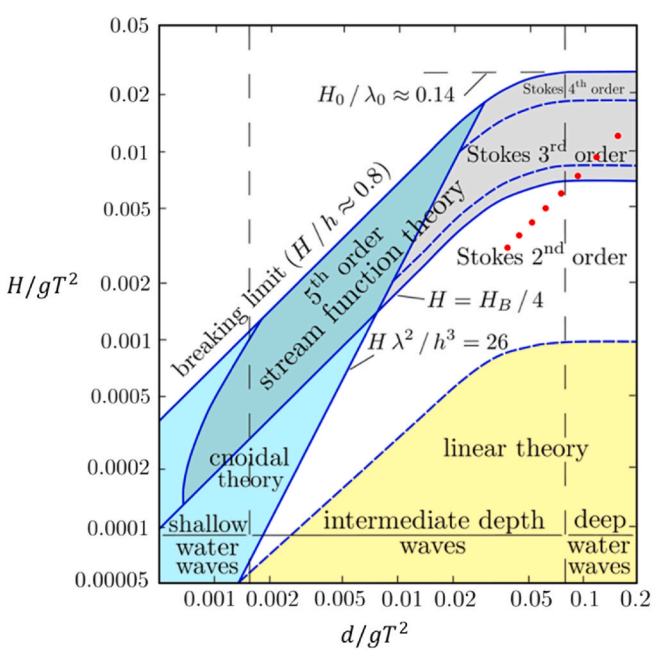

Fig. 2. Validity fields of wave theories according to (Le Méhauté, 2013). Red dots represent the wave conditions in this study.

the paper is organised as follows, Section 2 introduces the principal dimensions of the target WEC and the wave conditions. Section 3 describes the numerical modelling. Section 4 presents how to derive the analytic solution of the stationary wave due to the breakwater. Section 5 shows the result of validation and verification, the result of cases without breakwater and the result of cases with breakwater, while the conclusion is written in Section 6.

2. Geometry and conditions

2.1. Target wave energy converter

The target wave energy converter in this study is a Wavestar-like device which is considered a pivoted point absorber WEC. The Wavestar WEC consists of a hemisphere-shaped buoy with a single operational degree-of-freedom (DOF) in pitch motion and a hydraulic power take-off (PTO) cylinder (Ransley et al., 2017). Fig. 1 shows the schematic view of the buoy and the PTO cylinder, and the physical properties of the target WEC are presented in Table 1. Point A in Fig. 1 is the centre of rotation of the arm connected to the buoy and the buoy has a pitch motion following the fixed-point A. The displacement of the cylinder is determined by the distance between points B and C which are a fixed point and a moving point according to the position of the WEC device, respectively. In this study, the PTO system is not modelled in the CFD simulation to match the same conditions as this of the experiment in Ransley et al. (2017). In order to build a PTO system on a numerical simulation, the information of the coordinates of point C is needed every time step and but, in this study, establishing the PTO system on the present numerical simulation is not included and the research.

2.2. Wave conditions

The numerical simulations were performed at eight different wave conditions, as listed in Table 2. The wave period of the investigated wave conditions ranged from 1.4 s to 2.8 s. The wave height and water depth in the numerical simulations were 0.25m and 3.0m, respectively. Fig. 2 shows the validity of wave theories (Le Méhauté, 2013) according to wave period, wave height and water depth. The investigated wave conditions which are indicated as red dots in Fig. 2 ranged from Stokes 2nd order to Stokes 3rd order.

3. Numerical modelling

3.1. Governing equations

An unsteady Reynolds-Averaged Navier-Stokes (URANS) method was used to solve the governing equations, including the mass and momentum of conservation using the commercial CFD software Star-CCM+, version 15.04. The averaged continuity and momentum equations for unsteady incompressible flows without body forces are expressed in tensor notation and Cartesian coordinates as follows (Ferziger et al., 2002):

$$\frac{\partial(\rho\overline{u_i})}{\partial x_i} = 0 \tag{1}$$

$$\frac{\partial(\rho\overline{u_i})}{\partial t} + \frac{\partial}{\partial x_j}\left(\rho\overline{u_i}\,\overline{u_j} + \rho\overline{u_i'u_i'}\right) = -\frac{\partial\overline{p}}{\partial x_i} + \frac{\partial\overline{\tau}_{ij}}{\partial x_j} \tag{2}$$

in which $\overline{\tau}_{ij}$ are the mean viscous stress tensor components, as shown in Eq. (2)

$$\overline{\boldsymbol{\tau}}_{ij} = \boldsymbol{\mu}\left(\frac{\partial\overline{\boldsymbol{u}}_i}{\partial \boldsymbol{x}_j} + \frac{\partial\overline{\boldsymbol{u}}_j}{\partial \boldsymbol{x}_i}\right) \tag{3}$$

and p is the mean pressure, $\overline{u}_i$ is the averaged Cartesian components of the velocity vector, $\rho\overline{u_i'u_i'}$ is the Reynolds stresses, ρ is the fluid density

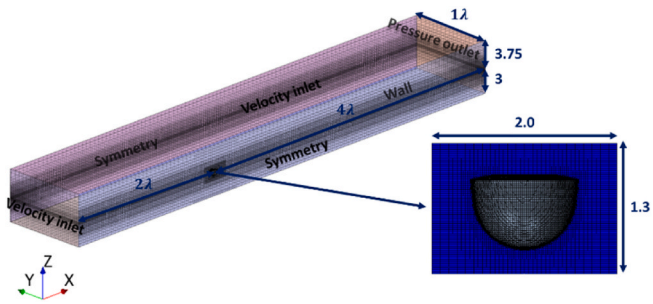

Fig. 3. The computational domain with imposed boundary conditions for numerical simulation cases without breakwater. The units on the figure are metres).

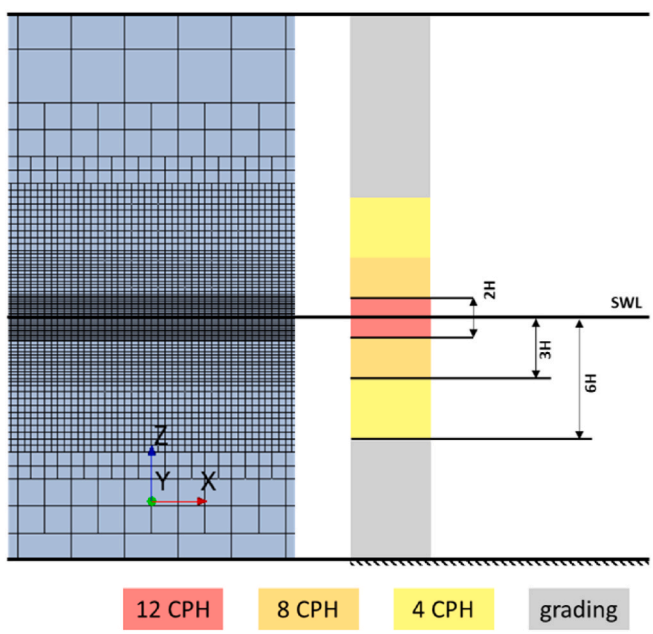

Fig. 4. The cells around the free surface (left) and the distribution of cells along the z-direction (right): Different colours represent different cells per wave height (CPH).

and μ is the dynamic viscosity.

In order to compute the fluid flow in the computational domain, the RANS solver uses a finite volume method that discretises the integral formulation of the governing equations. The continuity and momentum equations were solved in a sequential manner with a predictor-corrector approach. For spatial, a second-order upwind scheme was applied to convection and diffusion terms and for temporal, a second-order temporal discretization was used. A semi-implicit method for pressure linked equations (SIMPLE) algorithm was used to solve the pressure velocity coupling.

A Realizable $k-\varepsilon$ turbulence model was chosen in this study, which is generally used in many types of numerical simulations in ocean engineering. The two-layer approach, first suggested by (Rodi, 1991), is also included in the turbulence model to consider low Reynolds number type meshes $y^+ \sim 1$ or wall-function type meshes $y^+ > 30$. The range of the Reynolds number in this study is from 1.5×10^6 to 3.4×10^6 and this flow can be considered in a turbulent regime. In order to numerically model the motion of the WEC in response to external wave forces and moments, the dynamic fluid body interaction (DFBI) scheme was applied to the WEC which allows the pitch motion. The DFBI scheme can calculate the hydrodynamic forces and moments acting on the rigid body and solve the governing equations of the rigid body motion to determine the next position of the rigid body for the next time step. The volume of fluid technique, proposed in (Hirt and Nichols, 1981) is used to define the free surface (here, air-water interface). This VOF method allows capturing the free surface around the WEC and the regular waves in the computational domain.

3.2. The computational domain and boundary conditions

The computational domain was generated by a commercial software package of STAR-CCM+, which generally uses the Cartesian cut-cell method. There are two different domains for the pivoted WEC simulation in this study. Fig. 3 shows the size of the computational domain and selected boundary conditions for without breakwater cases which consist of a background mesh region and an overset mesh region around the buoy. For the boundary conditions for the background mesh region, a velocity inlet boundary condition, in which the distribution of velocity and fluid properties are known was set in the inflow boundary. The horizontal and vertical velocities and surface elevation for the inflow properties are calculated based on a fifth-order wave model by (Fenton, 1985). A symmetry plane is placed in the centre of the WEC device, to reduce the computational resources. A pressure outlet condition was imposed at the outflow boundary. For the buoy of the WEC system, no-slip wall boundary condition was used. To avoid the reflection wave from the boundaries in the computational domain and the distorted wave due to the motion of WEC around inflow, a wave forcing scheme mentioned in (Kim et al., 2012) was implemented and applied to the inflow and outflow boundaries. In the zone of wave forcing scheme, the solution of discretised transport equations is forced gradually into the forced solution or theoretical solution of the fifth-order wave model according to the distance to the inflow boundary. The initialised solution at the beginning of the numerical simulation can be seen in Fig. 5.

A dynamic overset mesh technique was used to investigate the motions of the WEC model. This technique can be used to capture the body motion and interaction with the surrounding fluids. A minimum of two independent mesh regions is required for setting up the overset mesh technique. In this study, the computational domain consists of the background mesh region for simulating a regular wave and overset mesh region for cutting a hole out of the background mesh region and representing a body interaction.

To simulate the regular waves in the background region, a minimum of 12 cells per wave height and 100 cells per wavelength near the still water line were generated for avoiding numerical dissipation. The finest resolution of cells covers one wave height below and above the still water line. The more detailed information related to the resolution of the cells along the z-direction can be found in Fig. 4.

Fig. 6 shows the computational domain for numerical simulations with breakwater. To avoid the reflection of wave due to the breakwater and the reach of the waves to inflow boundary, the length between inflow boundary and the body is relatively longer than the computation domain for cases without breakwater. The finest meshes covers the area between the body and breakwater because the wave run-up effect including diffracted and reflected wave are expected.

In a numerical simulation with a free surface including two-phase flow based on the Navier-Stokes equations, a remarkable effort must be made to reduce undesired wave reflections at the computational domain boundaries. The simplest and easiest way to eliminate the reflected waves generated in the computational domain boundaries is to increase the computational domain size. However, this will also lead to a significant increase in the computer resources and the simulation time. In addition, methods for reducing the reflected waves including beach (Lal and Elangovan, 2008), grid damping (Kraskowski, 2010; Peric and Abdel-Maksoud, 2015), solution forcing or coupling (Kim et al., 2012, 2013) and damping layer approaches (Choi and Yoon, 2009; Ha et al., 2011), and further approaches have been developed. Brief descriptions of the methods can be found in (Perić and Abdel-Maksoud, 2016). In this study, because of the breakwater in the computational domain, the wave

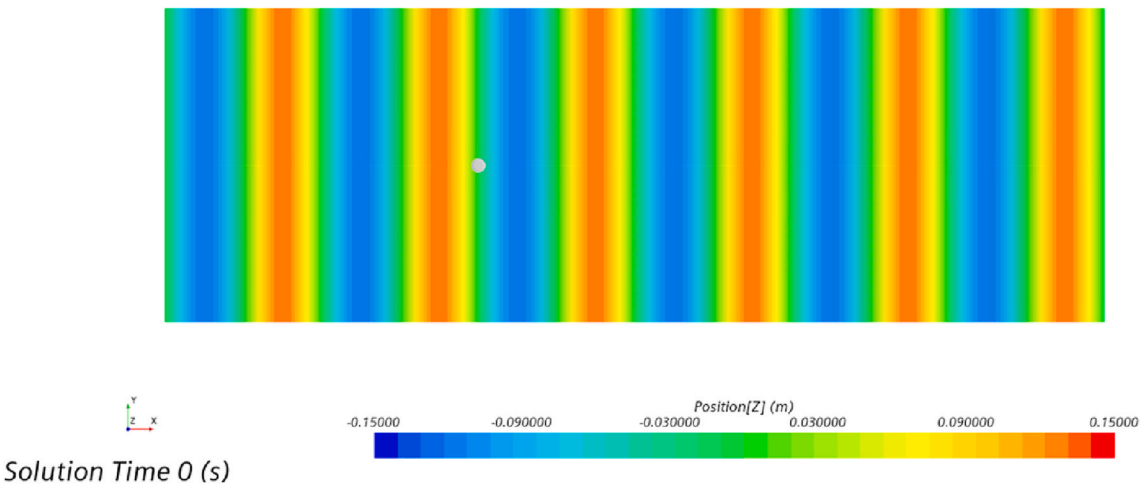

Fig. 5. Initialised computational domain before a numerical simulation starts.

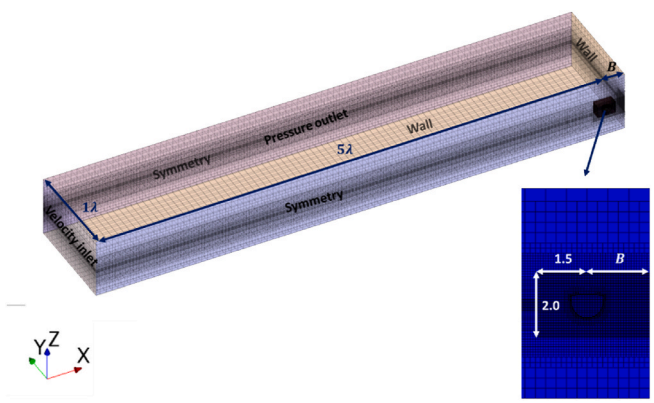

Fig. 6. The computational domain with imposed boundary conditions for with breakwater cases (Unit: m).

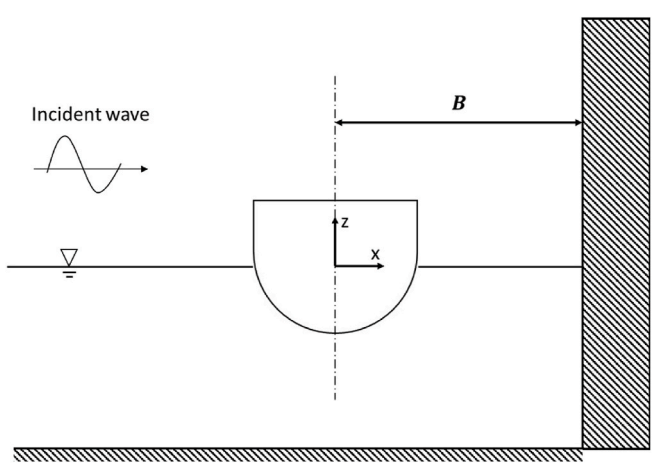

Fig. 7. Schematic view of a buoy and a breakwater.

forcing scheme was used among the various methods of the elimination of the reflected waves.

4. Stationary wave

Stationary wave, also known as standing wave, is combination of two identical waves moving in opposite directions. This phenomenon can be seen as a wave superposition and can be used to maximise the displacement of buoy in wave height direction. In a breakwater simulation case, a reflected wave due to the presence of the breakwater and an incident wave at inlet yield a stationary wave around the position of

Table 3
Calculation of the discretization error for the grid-spacing convergence study. (N: the number of grids, r: refinement ratio, φ: the solution of the averaged amplitude of the displacement of cylinder of WEC, more detailed information of the parameters including subscript and superscript can be found Section 5.1).

	Value
N_1	2,266,456
N_2	824,604
N_3	297,978
r_{21}	1.401
r_{32}	1.404
φ_1	0.0715
φ_2	0.0717
φ_3	0.0720
p	1.21
φ_{ext}^{21}	0.0712
e_a^{21}	0.2%
e_{ext}^{21}	0.5%
GCI_{fine}^{21}	0.6%

Table 4
Calculation of the discretization error for time-step convergence study.

	Value
Δt_1	0.0055
Δt_2	0.0077
Δt_3	0.0109
r_{21}	1.4142
r_{32}	1.4142
φ_1	0.0715
φ_2	0.0717
φ_3	0.0719
p	1.72
φ_{ext}^{21}	0.0714
e_a^{21}	0.2%
e_{ext}^{21}	0.2%
GCI_{fine}^{21}	0.3%

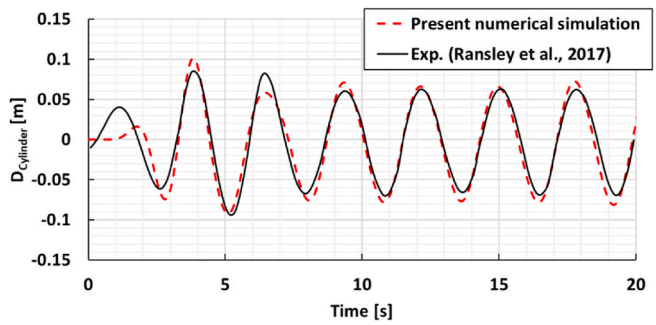

Fig. 8. Comparison of the displacement of cylinder between the simulated and experimental data (Ransley et al., 2017), T = 2.8s, H = 0.25m.

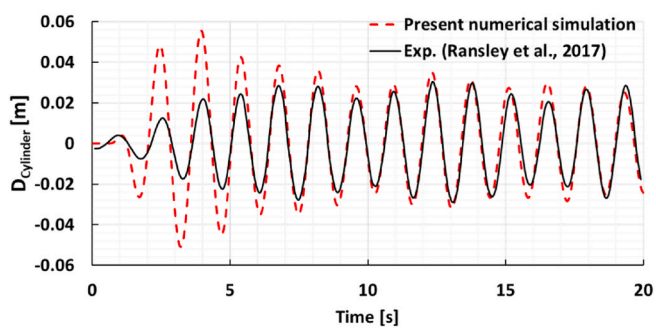

Fig. 9. Comparison of the displacement of cylinder between numerical simulation and experimental data (Ransley et al., 2017), T = 1.4s, H = 0.15m.

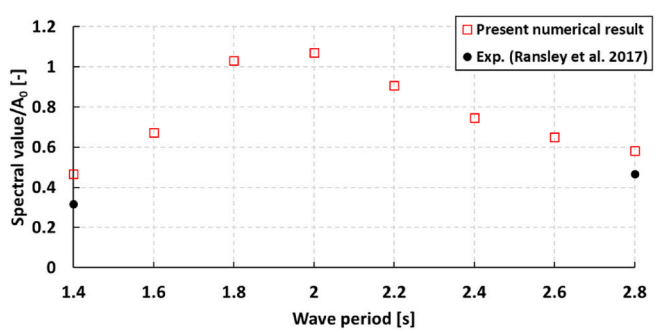

Fig. 10. Numerical results of FFT analysis of displacement of cylinder normalised by amplitude of incident wave and comparison result with experimental data (Ransley et al., 2017), A_0 represents the amplitude of undisturbed incident wave.

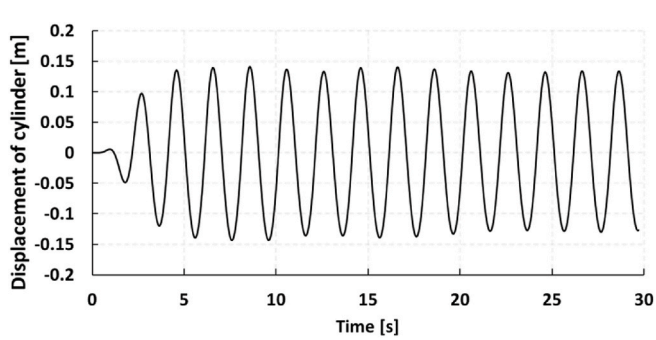

Fig. 11. Numerical displacement of cylinder data for wave case 4 without breakwater.

the buoy. Fig. 7 shows the brief view of the buoy and the breakwater and the origin of the coordinates is in the centre of the buoy in longitudinal direction at still water level. A wave travelling along the +x direction is reflected at the breakwater. An incident wave and a reflected wave can be described as a function of position x and t in Equation (4) and (5), respectively.

$$z_I(x,t) = z_{max}\sin(kx - \omega t) \tag{4}$$

$$z_R(x,t) = z_{max}\sin(kx + \omega t) \tag{5}$$

where z_{max} is amplitdue of incident wave, k is a wave number ($2\pi/\lambda$), and ω is a wave frequency ($2\pi/T$). To consider a distance to the breakwater, unknown quantity (C) is added in the Equation (5) to consider a reflection wave with a different phase due to distance to the breakwater and a variant reflected equation is derived as Equation (6).

$$z_R(x,t) = z_{\max}\sin(kx + \omega t + C) \tag{6}$$

$$z(x,t) = z_I(x,t) + z_R(x,t) = z_{\max}\sin(kx - \omega t) + z_{\max}\sin(kx + \omega t + C) \tag{7}$$

$$z(x,t) = 2z_{\max}\sin\left(kx + \frac{C}{2}\right)\cos\left(\omega t + \frac{C}{2}\right) \tag{8}$$

Using the trigonometric sum-to-product identity, the sum of the incident and reflected wave can be derived as Equation (8). At $x = B$ where the intersection point between SWL and the breakwater, since the maximised wave height is captured, the absolute value of sine term in Equation (8) should be maximised. Consequently, the equation (12) is derived when $x = 0$ where the buoy is located in a computational domain.

$$kB + \frac{C}{2} = \frac{n\pi}{2}\ (n = 1, 3, 5, \ldots)\ at\ x = B \tag{9}$$

$$C = n\pi - 2kB \tag{10}$$

$$z(x,t) = 2z_{\max}\sin\left(kx + \frac{n\pi}{2} - kB\right)\cos\left(\omega t + \frac{n\pi}{2} - kB\right) \tag{11}$$

$$z(t)_{x=0} = 2z_{\max}\sin\left(\frac{n\pi}{2} - kB\right)\cos\left(\omega t + \frac{n\pi}{2} - kB\right) \tag{12}$$

$$f(k,B) = \left|2z_{\max}\sin\left(\frac{n\pi}{2} - kB\right)\right| \tag{13}$$

In accordance with Equation (12), the analytic solution of the wave height at $x = 0$ depending on the wave period and the distance to the breakwater (B) can be obtained. The amplitude of Equation (12) means the maximum amplitude of the stationary wave equation, consequently, the analytic solution of the stationary wave considering incident and reflected wave due to the breakwater is obtained (Equation (13)). A more detailed discussion of the analytic solution and comparison results on the numerical results is described in Section 5.3.2.

5. Results

5.1. Verification and validation

In this study, the influence of changing the number of iterations on the numerical simulations was deemed to be negligible since the number of iterations was over 10. A verification study was carried out for the lower frequency wave case (Case 8) for grid-space and time-step uncertainties.

The procedure for estimation of discretization error followed the Grid Convergent Index (GCI) approach of Celik et al. (2008) based on the Richardson extrapolation method (Richardson, 1911). The definition and symbol of parameters in the verification study are the same as those used in Celik et al. (2008).

Let N and h denote the total number of grids for a numerical simu-

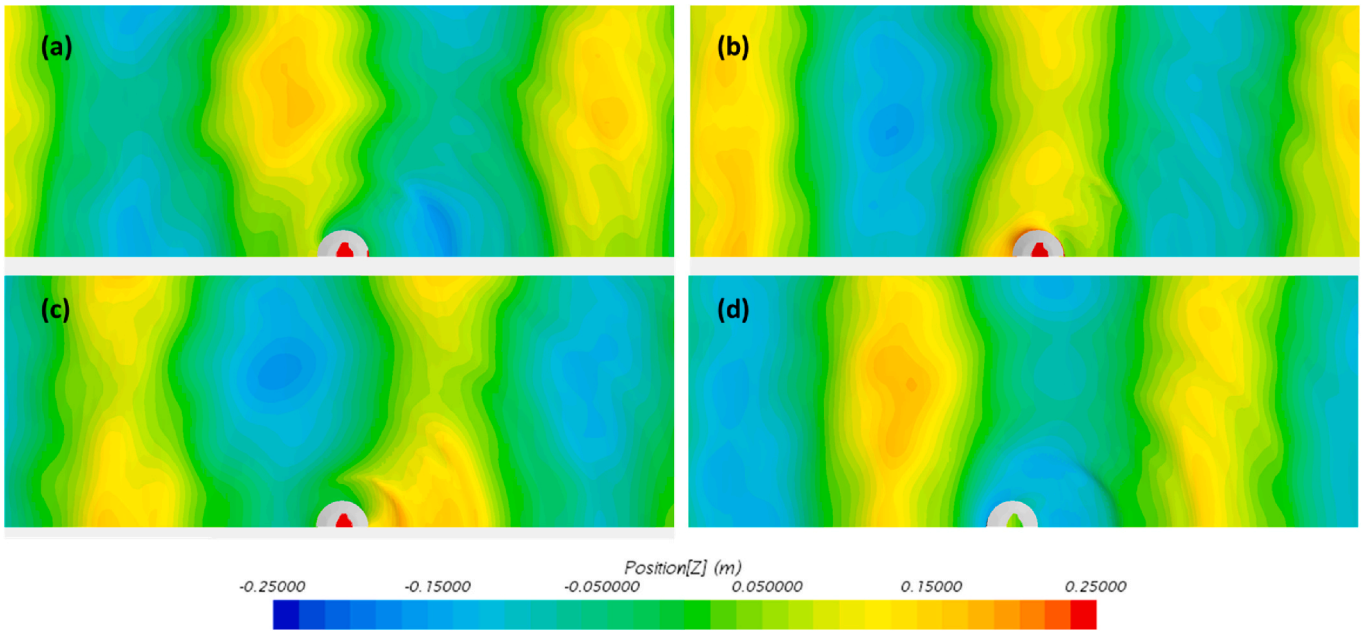

Fig. 12. Variation of the free surface around the buoy at 4 instants along a time period, top view. (Wave case 4: T = 2.0s, H = 0.25m).

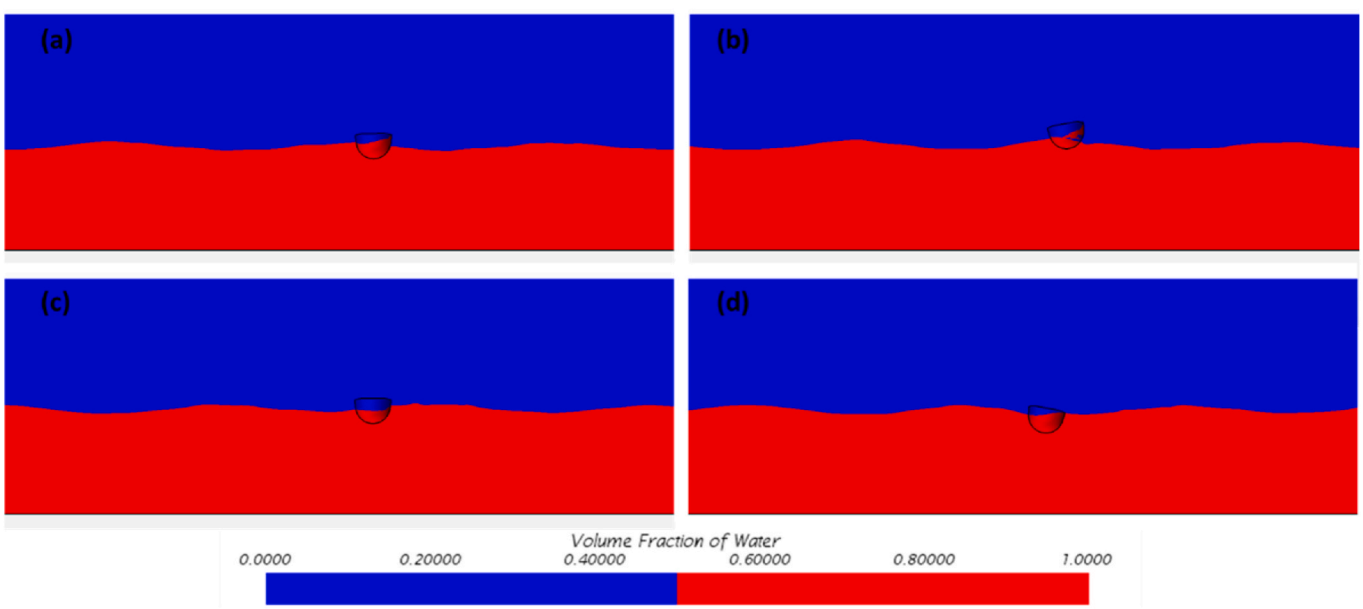

Fig. 13. Variation of the free surface around the buoy at 4 instants along a time period, side view. (Wave case 4: T = 2.0s, H = 0.25m).

lation and representative grid size, respectively, which gives the following expression:

$$h = \left[\frac{1}{N}\sum_{i=1}^{N}(\Delta V_i)\right]^{1/3} \tag{14}$$

$$r_{21} = h_2/h_1 \tag{15}$$

$$r_{32} = h_3/h_2 \tag{16}$$

where ΔV_i is the volume of the i th grid used for the simulation and r is the grid refinement factor defined by the ratio of the representative grid sizes. For a time-step convergence study, the definition of the time refinement factor can be given by $\gamma_{21} = \Delta t_2/\Delta t_1$ and $\gamma_{32} = \Delta t_3/\Delta t_2$. It is desirable that the refinement factor (r) be greater than 1.3 based on experience and not formal derivation according to Celik et al. (2008).

The apparent order of the method, p, can be solved using fixed-point iteration:

$$p = \frac{1}{\ln r_{21}}\left|\ln\left|\varepsilon_{32}/\varepsilon_{21}\right| + q(p)\right| \tag{17}$$

$$q(p) = \ln\left(\frac{r_{21}^p - s}{r_{32}^p - s}\right) \tag{18}$$

$$s = 1 \bullet sgn\left(\frac{\varepsilon_{32}}{\varepsilon_{21}}\right) \tag{19}$$

where $\varepsilon_{32} = \varphi_3 - \varphi_2$, $\varepsilon_{21} = \varphi_2 - \varphi_1$, and φ_k denotes the solution on the k th grid. Note that $q(p) = 0$ for $r = const$. The extrapolated values are calculated from

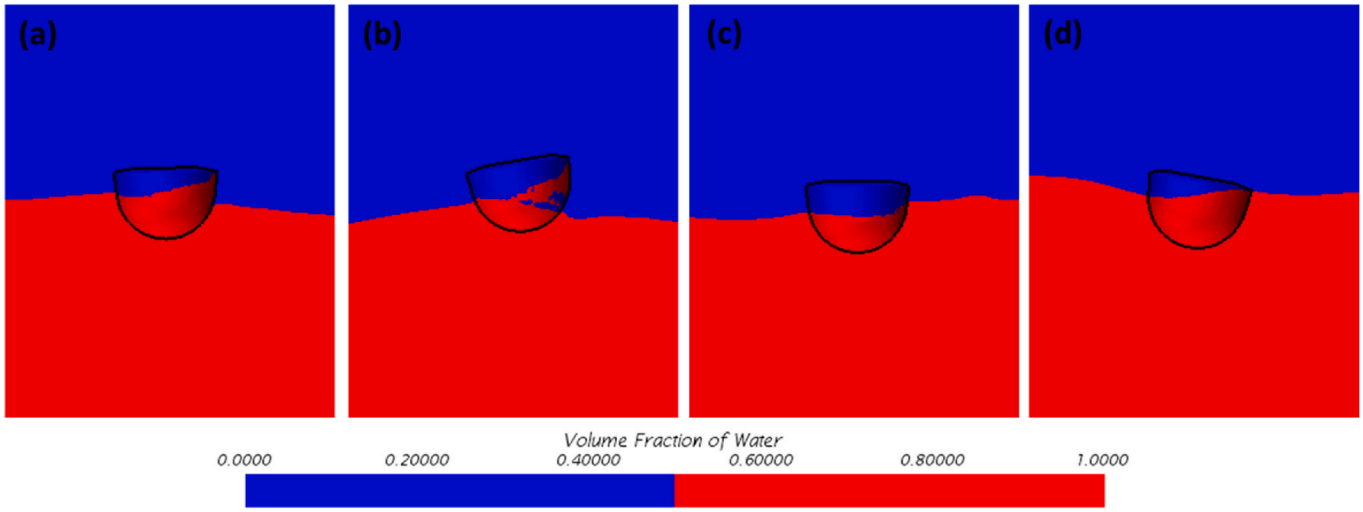

Fig. 14. Variation of the free surface nearby the buoy and on the wall of the buoy at 4 instants along a time period, side view. (Wave case 4: T = 2.0s, H = 0.25m).

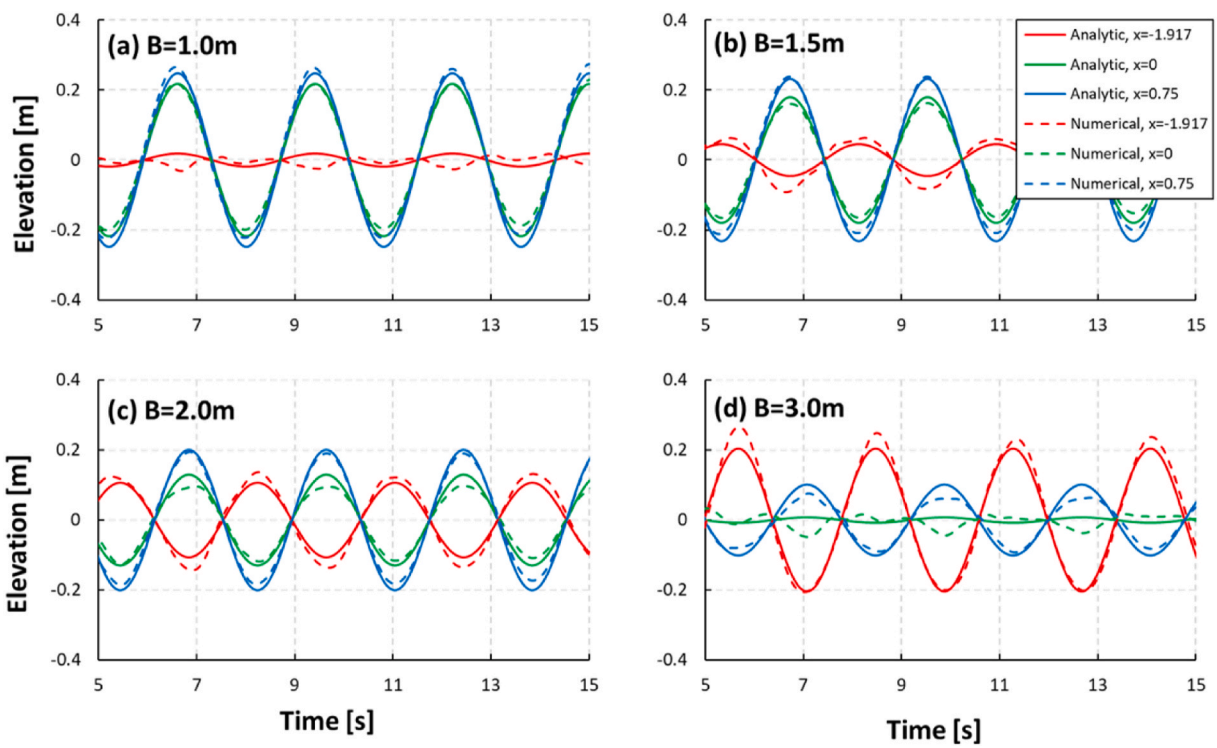

Fig. 15. Numerical data and analytic solution for wave case 8 at three different wave probes.

$$\varphi_{ext}^{21} = (r_{21}^{p}\varphi_1 - \varphi_2) \,/\, (r_{21}^{p} - 1) \tag{20}$$

The approximate relative error and extrapolated relative error, respectively, are described:

$$e_a^{21} = \left|\frac{\varphi_1 - \varphi_2}{\varphi_1}\right| \tag{21}$$

$$e_{ext}^{21} = \left|\frac{\varphi_{ext}^{21} - \varphi_1}{\varphi_{ext}^{21}}\right| \tag{22}$$

Finally, the fine-grid convergence index is calculated:

$$GCI_{\text{fine}}^{21} = \frac{1.25 e_a^{21}}{r_{21}^{p} - 1} \tag{23}$$

5.1.1. Grid-spacing convergence study

Case 8 (T = 2.8s, H = 0.25m) was selected for the grid-spacing convergence study. The grid-spacing convergence study was performed with three different grids, which are regarded as fine, medium, and coarse grids corresponding to grid numbers of 2,266,456 cells, 824,604 cells, and 297,978 cells, respectively. Table 3 shows the calculation procedure for the three different grids. As can be seen from the results of Table 3, the numerical uncertainties of 0.6% was estimated for the displacement of cylinder.

5.1.2. Time-step convergence study

The same wave case (Case 8) of the grid-spacing convergence study was selected for the time-step convergence study. Three different time-steps were employed with a uniform refinement ratio (r) of $\sqrt{2}$, starting

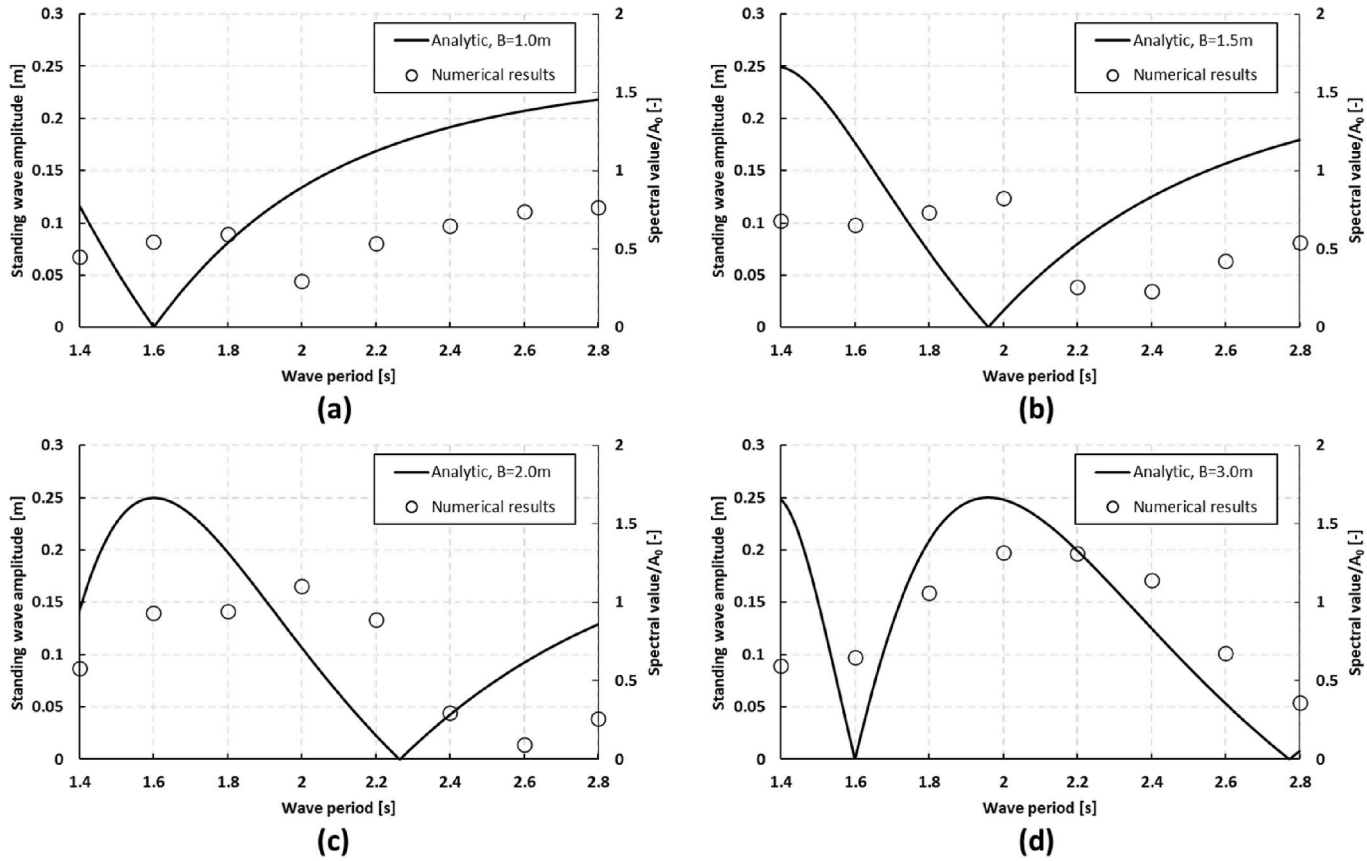

Fig. 16. Comparison between stationary wave amplitude and normalised spectral value of displacement of cylinder according to distance to breakwater (B). (A_0: amplitude of incident wave).

Table 5
Numerical result of the first harmonic component of cylinder displacement according to distance to breakwater (B).

Wave case, C	First harmonic component			
	B = 1.0m	B = 1.5m	B = 2.0m	B = 3.0m
1	0.0566	0.0851	0.0723	0.0741
2	0.0683	0.0817	0.1163	0.0814
3	0.0741	0.0920	0.1179	0.1325
4	0.0367	0.1033	0.1377	0.1648
5	0.0667	0.0324	0.1113	0.1641
6	0.0811	0.0290	0.0371	0.1424
7	0.0923	0.0532	0.0119	0.0845
8	0.0956	0.0678	0.0324	0.0449

from $\Delta t = T/512$. Table 4 shows the result of the calculation of the temporal discretization error. As can be seen from the result listed in Table 4, similar to the grid-spacing convergence study, small levels of uncertainty were estimated for the displacement of cylinder.

5.1.3. Validation

The computational domain for a validation work including the parameters of grid size and time-step was selected by the process of verification results. For the validation of the present numerical model, the experimental data of the displacement of cylinder from Ransley et al. (2017) were compared with the result of the present numerical simulations.

Fig. 8 shows the comparison of the displacement of cylinder between the present numerical simulation and experimental data from Ransley et al. (2017). The target wave for the validation work is the same as Wave Case 8 (wave period of 2.8 s and wave height of 0.25m). It should be noted that a positive displacement corresponds to a lifting of the buoy. The solid black line indicates the experimental data of the displacement of cylinder (Ransley et al., 2017) and the red dotted line indicates the present numerical simulation. Relatively large fluctuations with slightly different phase in the beginning of the numerical simulation are shown in Fig. 8. It is likely that the initial condition with fully developed wave field in the numerical model shown in Fig. 5 would affect the large amplitude of the motion. However, after around 10 s the numerical WEC device is beginning to oscillate with the same frequency as that found in their experiments and the displacement of cylinder for the numerical model shows good agreement with that of their experimental data.

Fig. 9 shows the comparison of the displacement of the cylinder between the numerical simulation and experimental data (Ransley et al., 2017) when the target wave period is 1.4 s and the wave height is 0.15m. Before comparing the experimental results with the present CFD results, Ransley et al. (2017) mentioned that the low-frequency beating of the displacement was captured due to the reflected waves in the physical basin at short wavelength. The low-frequency beating of the displacement indicates that the amplitude of the displacement of cylinder keep increasing and decreasing. This beating behaviour was not captured at long wavelength. Similarly, the present numerical result shows the same pattern of the low-frequency beating but the amount of the beating is relatively lower than that of their experimental data. It can be found that the low-frequency beating would be related to not only the reflected wave due to a wall in the physical basin but also a diffraction wave around the WEC device. As with the previous validation case, because of the initial condition of the computational domain results in the large amplitude of the motion of the WEC device in the beginning part. Overall good agreement between the present numerical and experimental (Ransley et al., 2017) results is observed.

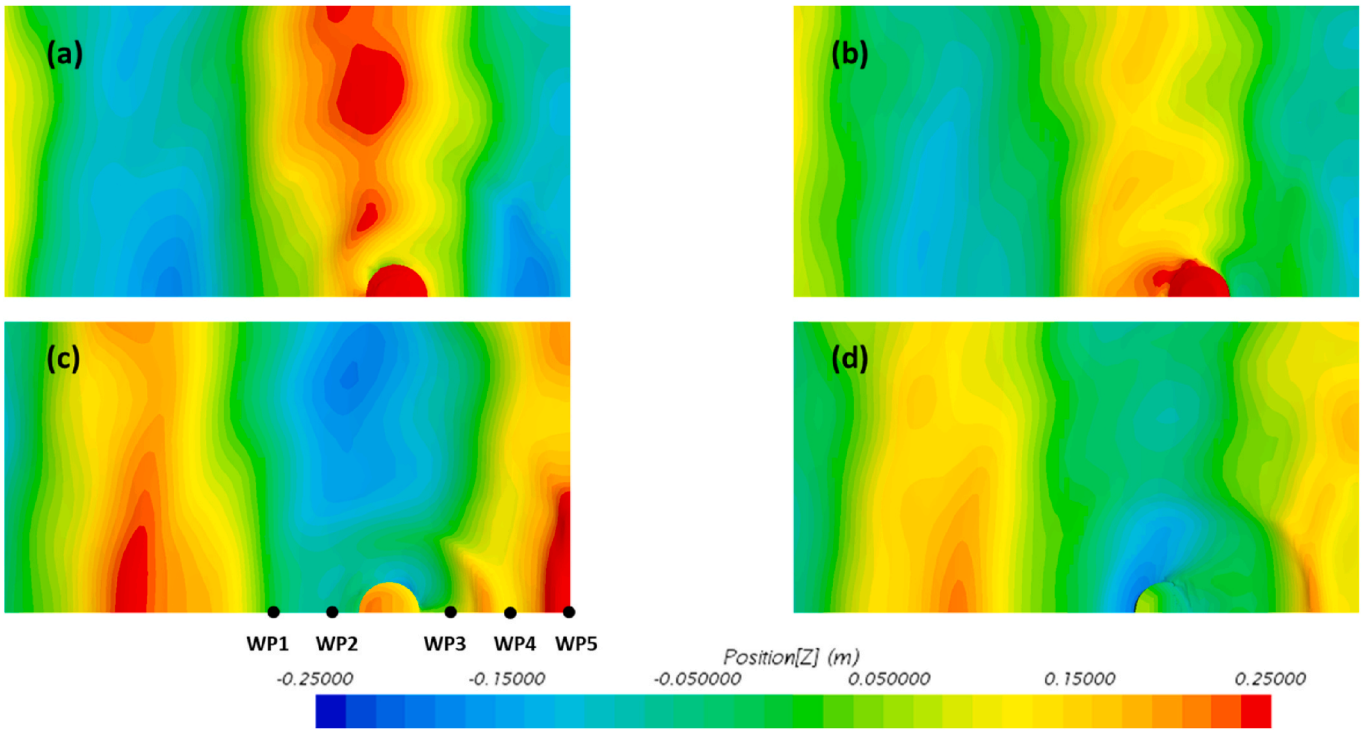

Fig. 17. Variation of the free surface around the buoy with breakwater, top view. And location of wave probes (Wave case 4: T = 2.0s, H = 0.25m and B = 3.0m).

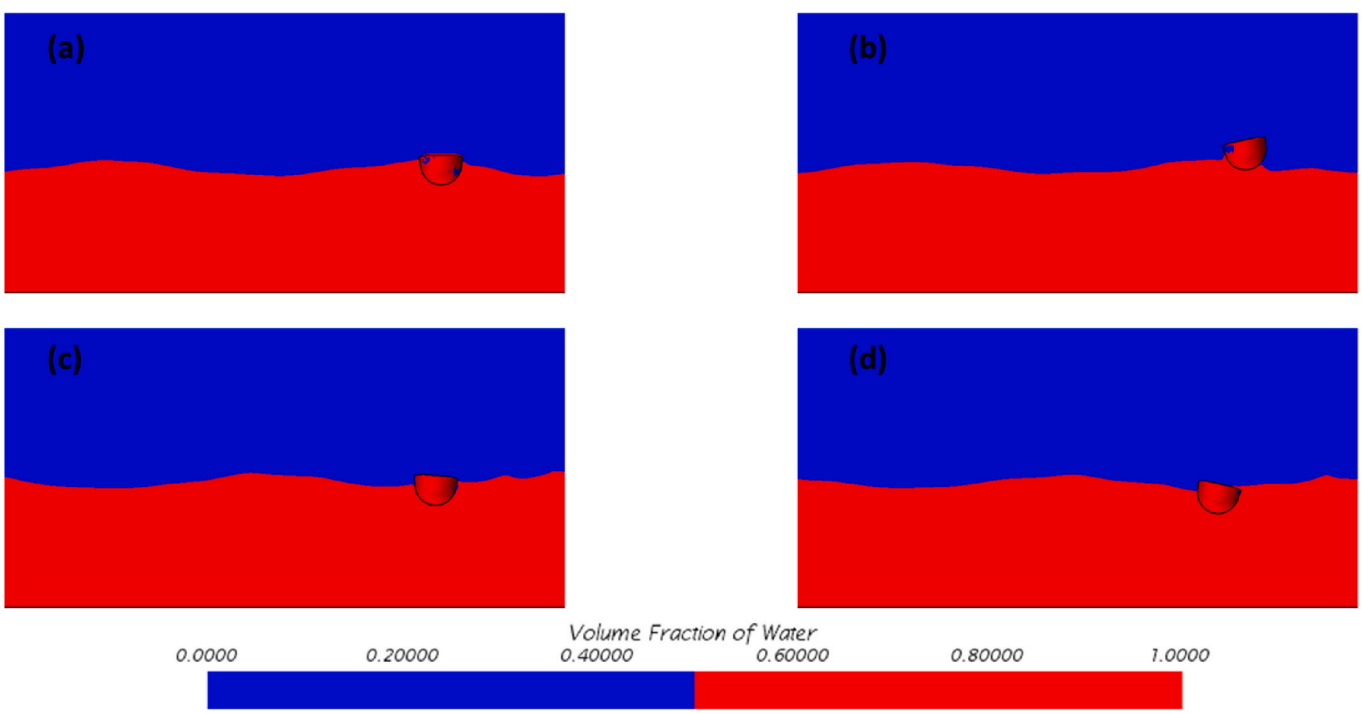

Fig. 18. Variation of the free surface around the buoy with breakwater, side view. (Wave case 4: T = 2.0s, H = 0.25m and B = 3.0m).

5.2. Cases without breakwater

Numerical simulations without a breakwater were investigated according to wave period. From the results of the numerical simulations without the breakwater, the characteristic of the target WEC according to wave period can be obtained such as a natural frequency and a response to an incident wave of the target WEC. For the analysis of the numerical simulations, the displacement of the cylinder, considering eight consecutive wave periods has been recorded and the recorded displacement has been analysed by fast the Fourier transform (FFT) method in order to obtain the first harmonic component. The first harmonic component was normalised by the amplitude of the incident wave and presented in Fig. 10. In addition, for comparison with the results of the experiment data (Ransley et al., 2017), the result values were included in Fig. 10. It can be found that the numerical simulation results are slightly overpredicted. Fig. 11 shows the time history of the

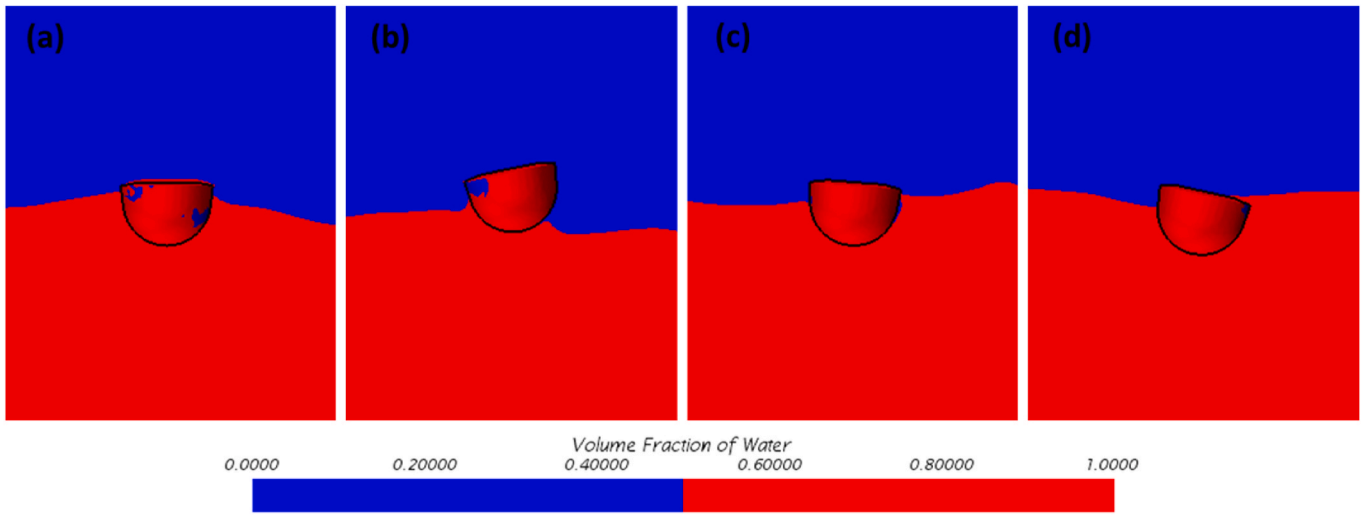

Fig. 19. Variation of the free surface nearby the buoy and on the wall of the buoy with breakwater, side view. (Wave case 4: T = 2.0s, H = 0.25m and B = 3.0m).

displacement of the cylinder for wave case 4 (T = 2.0s) for 30 s, which showed the largest WEC motion amongst the selected wave cases. After approximately 5 s the displacement of the cylinder in the numerical simulation begins to oscillate stably, and the data during the eight consecutive wave periods were selected for the FFT analysis. The largest motion is captured in wave case 4 (T = 2.0s) and a similar natural period of the WEC was captured in their previous experimental research (Jakobsen et al., 2016).

Fig. 12 shows the view of the free surface around the buoy in Case 4. It should be reiterated that the maximum displacement of the cylinder is observed in Case 4 amongst the selected wave cases in this study.

Figs. 12 and 13 show the free surface variation around the buoy for wave case 4 without breakwater, respectively, at 4 instants along a time period; (a) zero-up crossing of the displacement of the cylinder, (b) the maximum lift of the WEC device, (c) zero-down crossing of the displacement of the cylinder and (d) the minimum lift of the WEC device. The absolute value of the maximum and minimum range in a contour in Fig. 12 is the wave height of the incident wave. A wave crest propagating toward the WEC device can be seen in Fig. 12 (a) and this leads the maximum lift of the WEC device and then the generated and distorted wave due to the motion of the WEC device is observed in Fig. 12 (c) and (d).

Fig. 13 shows variation of the free surface on the symmetry plane in the computational domain. There are only 2 contour colours, which red colour indicates the water and blue indicates the air, to clearly identify the free surface. Fig. 14 shows the clear views of the free surface nearby the buoy and on the wall of the buoy. During the propagation of the incident wave, the change in the wet surface of the WEC device according to the position of the WEC device can be seen.

5.3. Cases with breakwater

5.3.1. Stationary wave analysis

A simplified analytic stationary wave equation was derived and compared to this study's CFD results. The free surface elevations from the analytical solution and the present numerical model are compared directly at three different wave probes (x = −1.917m, x = 0m, and x = 0.75m). The positive x-direction is towards the breakwater in the computational domain and x = 0 means the location where the buoy is located. For the comparison between the analytical solution and the present numerical model, the buoy was not installed to capture the stationary waves due to the breakwater.

Solid lines and dotted lines in Fig. 15 indicate the analytical solutions derived from Equation (11) and the numerical results, respectively. Different colours represent the location of the probe. For the case of B = 1.0m which is the shortest distance to the breakwater, overall good agreement between the analytical solution and the numerical data is observed except at x = −1.917m, as shown in Fig. 15 (a). A possible reason for the mismatch between the analytic and numerical results is that the amplitude of the free surface elevation is relatively too small to capture the superposed wave in the numerical simulation. Another possible reason can be that the analytical solution does not consider the higher order wave equations.

For the cases of B = 1.5m and B = 2.0m (Fig. 15 (b), (c)), the free surface elevation results obtained from the analytical solution and the numerical data match reasonably well, whereas slightly over- and under-prediction of the wave crests and troughs at x = −1.917m are found, respectively. For the case of B = 3.0m which is the longest distance to the breakwater in this study, a similar trend regarding the mismatch is found at x = −0.75m which is shown the small amplitude of free surface elevation (Fig. 15 (d)). As a result of the comparison in Fig. 13, it was thought that the analytical solution is reasonably accurate to calculate the amplitude of the free surface elevation around the location where the WEC buoy is located with the breakwater.

5.3.2. Cases with breakwater analysis

In this section, the results of numerical simulations with a breakwater and the analytical solutions discussed in Section 4.0 were compared. The first harmonic components by FFT analysis method were obtained, considering six consecutive wave periods of numerical simulations with the breakwater. In this case, it is highlighted that a relatively small amount of consecutive wave periods should be considered due to the possibility of a strongly distorted incident wave. Even though the wave forcing scheme works well near the inflow boundary, the possibility to occur the numerical error cannot be ignored. To find a correlation between the motion of WEC and stationary wave, the first harmonic components have been compared with the amplitude of the stationary wave.

Solid lines shown in Fig. 16 represent the result of the analytical solution based on Equation (13) and the circle symbol means the first harmonic component by FFT analysis. Table 5 shows the result of numerical solutions and comparison result, where B represents the distance to the breakwater. For $B = 1.0m$, which is the shortest distance to the breakwater, the amplitude of the stationary wave by analytical solution decreases rapidly, reaches the lowest point approximately at $T = 1.6s$, and then increases gradually. In the case of numerical results for $B = 1.0m$, the smallest value of the first harmonic component is captured at $T = 2.0s$. As the wave period increased from $T = 2.0s$, the first harmonic

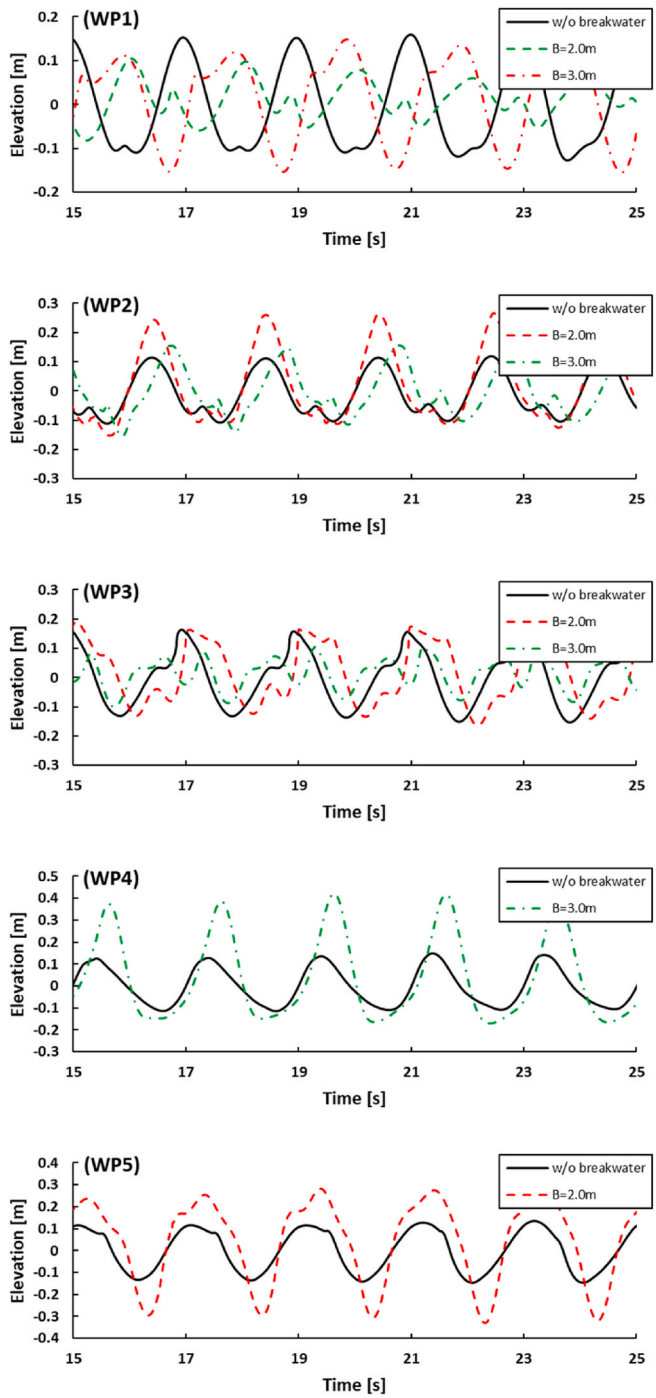

Fig. 20. Comparison of wave elevations for Wave case 4. Black solid line means the result of cases without breakwater, Red dashed line means the result of cases with breakwater (B = 2.0m) and Green dashed dot line represents the result of cases with breakwater (B = 3.0m).

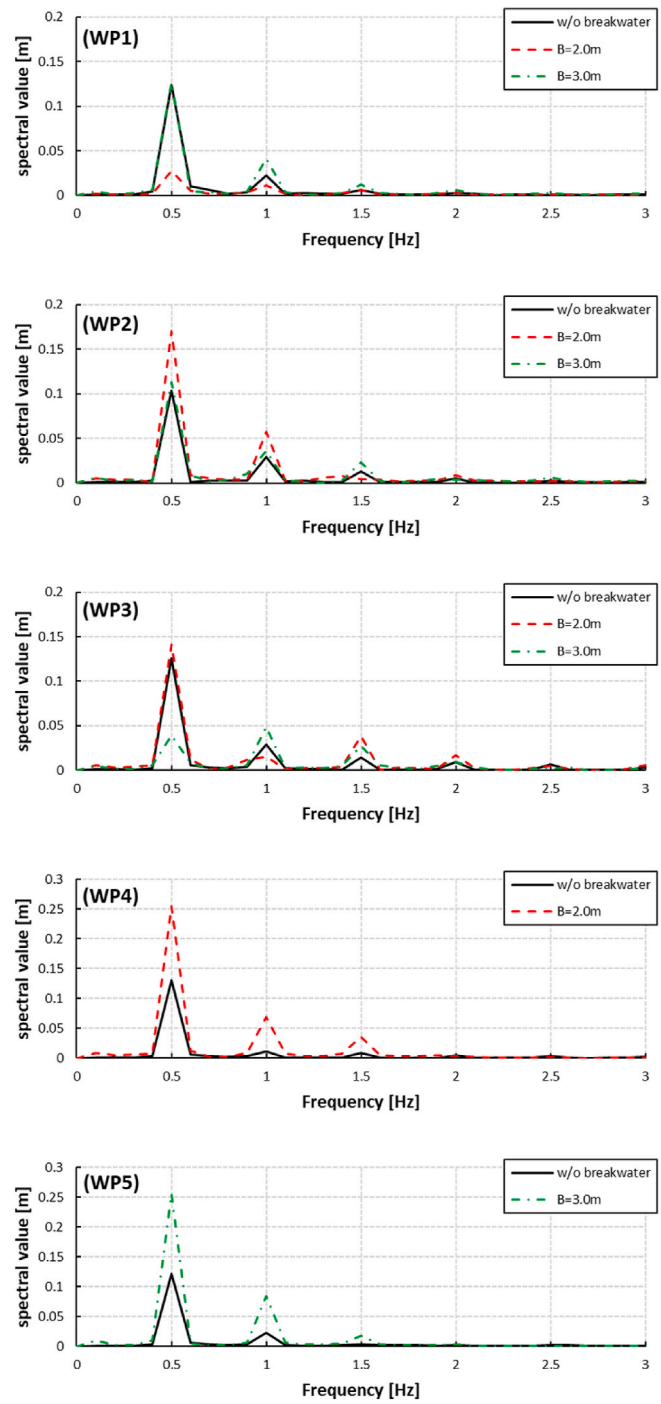

Fig. 21. Comparison of FFT results for Wave case 4 by wave probe. Black solid line means the result of cases without breakwater, Red dashed line means the result of cases with breakwater (B = 2.0m) and Green dashed dot line represents the result of cases with breakwater (B = 3.0m).

Table 6
Location of wave probes (WP).

Probe	WP1	WP2	WP3	WP4	WP5
x-coordinate [m]	−2.0	−1.0	1.0	2.0	3.0

component also tended to increase until T = 1.8s and then to decrease. In terms of the lowest point, it can be seen that the results of the analytical solution and CFD do not match, and this phenomenon can be seen, in a similar fashion, at different distances to the breakwater. One possible explanation can be that the analytical solution in this study considered only the reflection waves from the breakwater and the incident waves towards the breakwater, in order to simplify the equation, whilst the numerical model included diffracted, radiated, reflected waves with all non-linearities. Despite the ignorance of the complicated waves between the WEC buoy and the breakwater in the analytical solution, the result of the analytic solution appears similar to the trend of the numerical results.

For $B = 1.5m$ and $B = 2.0m$, the amplitude of the analytical solution

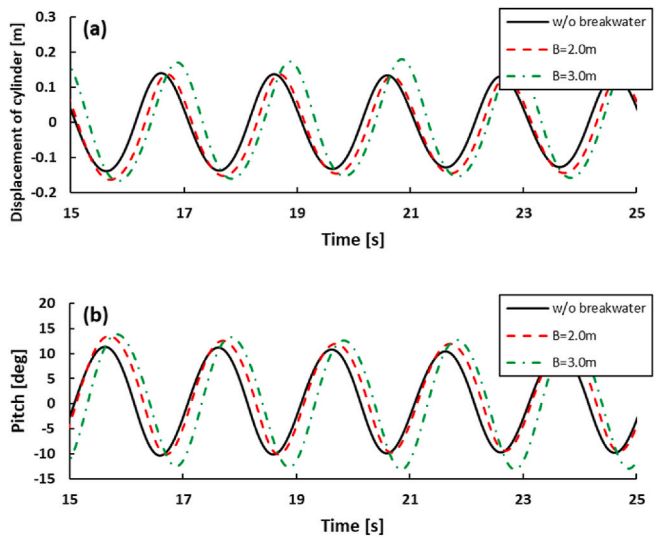

Fig. 22. Comparison of motion of WEC according to the presence of breakwater. (a): Displacement of cylinder, (b): pitch. Black solid line means the result of cases without breakwater, Red dashed line means the result of cases with breakwater (B = 2.0m) and Green dashed dot line represents the result of cases with breakwater (B = 3.0m).

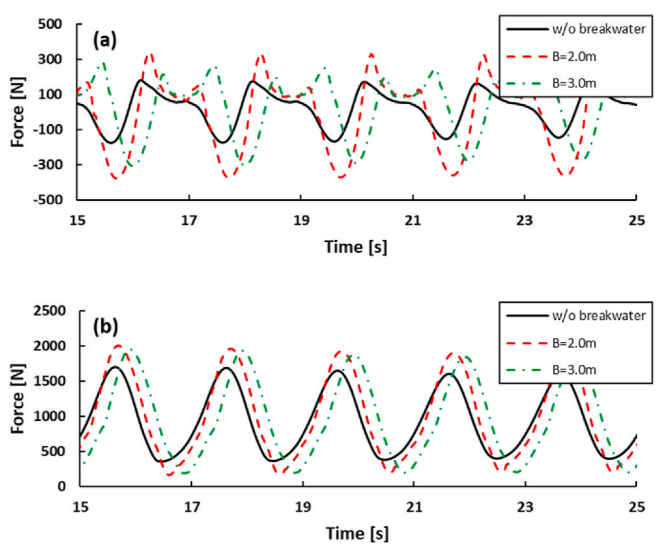

Fig. 23. Comparison of horizontal and vertical forces. (a): horizontal force, (b): vertical force. Black solid line means the result of cases without breakwater, Red dashed line means the result of cases with breakwater (B = 2.0m) and Green dashed dot line represents the result of cases with breakwater (B = 3.0m).

and the first harmonic component of the numerical result according to wave period can be seen in Fig. 16 (b). As in the case of $B = 1.0m$, the results of analytical solutions and numerical results show the similar trend in terms of the position of the lowest point. At T = 1.4s for $B = 1.5m$, the analytical solution shows the maximum stationary wave amplitude, and it is likely that the stationary wave caused the increase of the motion of the WEC device. Even in the short-wave period regime (i.e., T = 1.4s), which showed the lowest motion response in the numerical case without breakwater, the result of the first harmonic component increased by 41%.

For $B = 3.0m$, which is the longest distance to the breakwater, the amplitude of the analytical solution and the first harmonic component of the numerical result according to wave period can be seen in Fig. 16 (d). Except for the short-wave period regime, overall good agreement between the analytical solution and the numerical results is observed. In the case of $B = 3.0m$, the maximum stationary wave amplitude is distributed near the natural frequency of the WEC device and was expected to have a significant effect on the motion of the WEC device. As a result, the WEC device showed the highest response at T = 2s (near the natural frequency of the WEC device), which is 17% higher than that of the numerical case without the breakwater.

Generally, when comparing the results of the analytical solution and the numerical solution, it is similar to show a tendency to gradually increase after the lowest point of the motion response, but the biggest difference between the two results is the position where the lowest point is recorded. As the trend of the numerical results is also comparable to that of the analytical solution, it seems clear that the stationary wave has an effect on the results, but it is considered that accurate estimation is difficult since the analytical solution is composed of two waves components only. Nevertheless, the correlation between the breakwater distance and the motion of the WEC device could be estimated even with a simple analytic solution. It was confirmed that this can be suggested as a way to amplify the floating body motion according to the position of the breakwater.

Each scene of Figs. 17 and 18 shows the time instants of (a) zero-up crossing of the displacement of the cylinder, (b) the maximum lift of the WEC device, (c) zero-down crossing of the displacement of the cylinder and (d) the minimum lift of the WEC device when the wave period and wave height are 2.0 s and 0.25m, respectively, and the distance to breakwater (B) is 3.0m. Fig. 19 shows the clear views of the free surface nearby the buoy and on the wall of the buoy with breakwater. The right side of each scene is the location of the breakwater. More complicated wave distribution and higher wave amplitudes are captured in the numerical case with breakwater compared to those in without breakwater. It is noted that the WEC buoy has been covered with water due to the green water effect, the water elevation on the position of the WEC buoy has also increased and decreased. The wave run-up effect is also observed near the breakwater, where the free surface elevation reached two times of incident wave height.

Fig. 20 shows the change in wave elevation for Wave case 4 (T = 2.0s and H = 0.25m) according to each wave probe position. Probes of WP1 and WP2 are located in upstream of the WEC buoy and rest of probes (WP3-5) are in downstream of the WEC buoy. It should be noted that WP4 and WP5 are installed where the breakwater is located. The x-coordinate of the wave probe location can be seen in Table 6 and Fig. 17. The records of WP1 and WP2 in Fig. 20 show the change of the free surface in front of the WEC buoy. It can be seen that the changes of the free surface are more complicated when there is the breakwater than when there is no breakwater. This is because the reflected waves generated from the breakwater make the waves around the WEC buoy more disturbed. The records of WP3 in Fig. 20 show the change of the free surface in the downstream of the WEC buoy by 1.0m. In this case, in the wake region behind the object, a clearer change in waves can be seen depending on the presence of the breakwater. When there is the breakwater, the waves that may occur between the WEC buoy and the breakwater are as follow. It is organised into disturbed incident waves, radiation waves generated by the motion of the WEC buoy, reflected waves of the disturbed incident waves from the breakwater and reflected waves of the radiation waves. Due to these wave components, it is believed that more complicated waves are measured in the wave region behind the WEC buoy. The final two records (WP4 and WP5) show the changes of the free surface at the breakwater when the distance is B = 2.0m and B = 3.0m. The biggest difference is that the wave height has increased significantly due to the breakwater. And the wave height of the free surface in the breakwater is about twice the wave height of the incident wave.

In order to further investigate higher harmonic contributions around the WEC buoy, Fig. 21 shows a FFT analysis of the free surface records. At all wave probes, it was possible to confirm the first, second and third

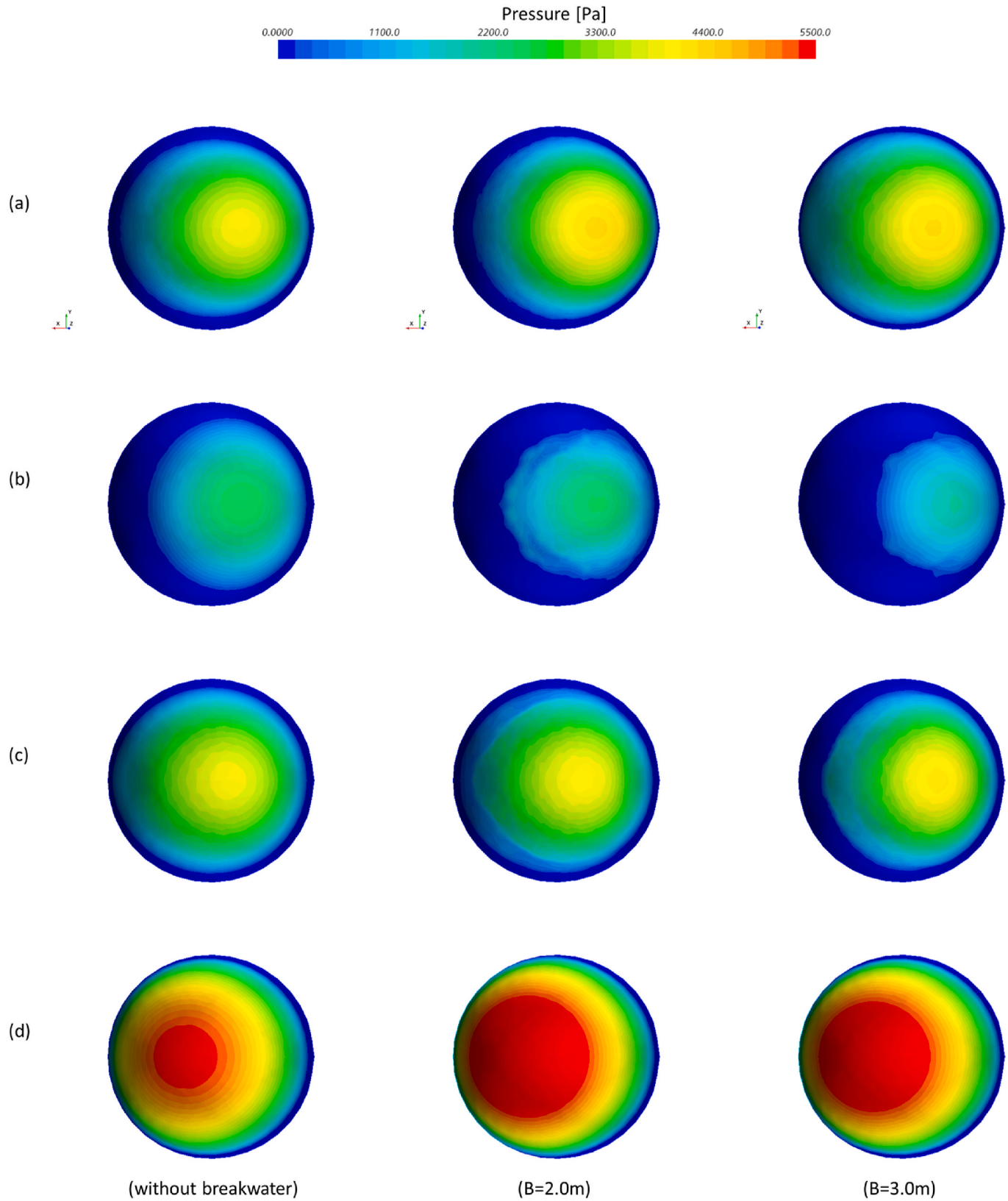

Fig. 24. Pressure distribution of the WEC buoy for Wave case 4 (T = 2.0s and H = 0.25m). Case without breakwater (the first column), case when B = 2.0m (the second column) and case when B = 3.0m (the third column). (a): zero-up crossing, (b): maximum lift, (c): zero-down crossing, (d): minimum lift.

harmonic components. In particular, in WP3 corresponding to wake region, higher harmonic components than the third harmonic can be observed.

Figs. 22 and 23 show the motion and forces on the WEC buoy, respectively. Each plot includes the result of the case without the breakwater, when B = 2.0m (the distance to the breakwater is 2.0m) and B = 3.0m. The positive of displacement of cylinder and represents the lifting of the WEC buoy above the still water level. The horizontal force graph shows relatively the larger difference between the present numerical results. It is interesting to note that the horizontal force on WEC buoy follows the similar trend of the displacement of cylinder. As a result, the combination of vertical and horizontal forces must have an effect on the displacement of cylinder, but it can be assumed that the influence of vertical force on the motion of WEC buoy is greater than the horizontal force.

Fig. 24 show the pressure distribution on the bottom of the WEC buoy. Each scene in Fig. 24 shows the time instants of (a) zero-up crossing of the displacement of the cylinder, (b) the maximum lift of the WEC buoy, (c) zero-down crossing of the displacement of the cylinder and (d) the minimum lift of the WEC buoy when Wave case is 4 (T = 2.0s and H = 0.25m) and distance to the breakwater is 2.0m (B = 2.0m). There are significant differences in the pressure distribution at time instants of (b) and (d). When the WEC buoy reaches at the maximum lift point, the shape of pressure distribution for B = 2.0m and B = 3.0m shows more complicated than that of the case without breakwater. The reason for this is thought to be that the location of the WEC buoy (e.g. displacement of cylinder) and the waves around the WEC buoy have become more sophisticated. Depending on how high the WEC buoy rises, the wetted surface area should change and the pressure distribution may change accordingly. Similarly, when the WEC buoy is down to its minimum lift point, it can be confirmed that a greater pressure is generated because the movement increases in the presence of a breakwater.

6. Conclusion

The work presented in this paper describes the validation of a numerical model of the pivoted WEC device with the available experimental data (Ransley et al., 2017) including the verification of the numerical model. In order to understand the hydrodynamic performance according to the distance between the breakwater and the WEC device, a total of four different distances to breakwater were set and the results were compared. To understand the stationary wave in the case with breakwater, an analytical solution which considers only the incident and reflected wave is derived. The maximum wave height by the analytical solution is compared with the numerical results via an FFT analysis to understand and find out the influence of the presence of the breakwater on the motions of the WEC body.

The validation of the numerical model has a good agreement with the published experimental data (Ransley et al., 2017) in two different wave period cases. Based on the validated numerical model, the motion response of the pivoted WEC body according to the distance to the breakwater has been investigated and the numerical model has captured well the changes of the motion response, by considering the effect of the stationary wave from the breakwater.

From the simple analytical solution, it was possible to predict the stationary waves around the breakwater, and how these stationary waves influence the WEC device, analysing the results of the numerical simulations. As a result, when the wave period is 1.4 s, the motion response to the waves increased by 41% compared to when there was no breakwater, and when the wave period was close to the resonance period of 2.0 s, it increased by 17%. Given the simplified assumptions of the analytical solution, it can be confirmed that the amplitude of the stationary wave is greatly related to the motion of the WEC body installed in the breakwater and help to find the optimisation result of the WEC device in terms of the distance to the breakwater. Regardless of effect of the stationary wave in front of the breakwater, waves induced by the movement of the buoy have significant influence on the hydrodynamic performance of the WEC. Using those numerical models, it helps to understand the hydrodynamic performance of the integration of the breakwater-WEC at certain environments. For a more practical outcome, integrating breakwater-WEC including PTO should be considered in the near future.

CRediT authorship contribution statement

Injun Yang: Conceptualization, Methodology, Software, Validation, Formal analysis, Investigation, Resources, Data curation, Writing – original draft, Writing – review & editing, Visualization, Supervision, Project administration. **Tahsin Tezdogan:** Writing – review & editing, Supervision, Project administration. **Atilla Incecik:** Writing – review & editing, Supervision, Project administration.

Declaration of competing interest

The authors declare that they have no known competing financial interests or personal relationships that could have appeared to influence the work reported in this paper.

Data availability

Data will be made available on request.

Acknowledgements

Results were obtained using the ARCHIE-WeSt High Performance Computer (www.archie-west.ac.uk) based at the University of Strathclyde.

References

Celik, I.B., Ghia, U., Roache, P.J., Freitas, C.J., Coleman, H., Raad, P.E., 2008. Procedure for estimation and reporting of uncertainty due to discretization in CFD applications. J. Fluid Eng. 130 (7) https://doi.org/10.1115/1.2960953, 0780011-0780014.

Chen, Q., Zang, J., Birchall, J., Ning, D., Zhao, X., Gao, J., 2020. On the hydrodynamic performance of a vertical pile-restrained WEC-type floating breakwater. Renew. Energy 146, 414–425. https://doi.org/10.1016/j.renene.2019.06.149.

Cheng, Y., Xi, C., Dai, S., Ji, C., Cocard, M., Yuan, Z., Incecik, A., 2021. Performance characteristics and parametric analysis of a novel multi-purpose platform combining a moonpool-type floating breakwater and an array of wave energy converters. Appl. Energy 292, 116888. https://doi.org/10.1016/j.apenergy.2021.116888.

Choi, J., Yoon, S.B., 2009. Numerical simulations using momentum source wave-maker applied to RANS equation model. Coast. Eng. 56 (10), 1043–1060.

Coiro, D.P., Troise, G., Calise, G., Bizzarrini, N., 2016. Wave energy conversion through a point pivoted absorber: numerical and experimental tests on a scaled model. Renew. Energy 87, 317–325. https://doi.org/10.1016/j.renene.2015.10.003.

Day, A.H., Babarit, A., Fontaine, A., He, Y.-P., Kraskowski, M., Murai, M., Penesis, I., Salvatore, F., Shin, H.-K., 2015. Hydrodynamic modelling of marine renewable energy devices: a state of the art review. Ocean Eng. 108, 46–69. https://doi.org/10.1016/j.oceaneng.2015.05.036.

Falcão, A.F.d.O., 2010. Wave energy utilization: a review of the technologies. Renew. Sustain. Energy Rev. 14 (3), 899–918. https://doi.org/10.1016/j.rser.2009.11.003 info:doi/10.1016/j.rser.2009.11.003.

Fenton, J.D., 1985. A fifth-order Stokes theory for steady waves. J. Waterw. Port, Coast. Ocean Eng. 111 (2), 216–234.

Ferziger, J.H., Perić, M., Street, R.L., 2002. Computational Methods for Fluid Dynamics, 3. Springer.

Guo, B., Wang, R., Ning, D., Chen, L., Sulisz, W., 2020. Hydrodynamic performance of a novel WEC-breakwater integrated system consisting of triple dual-freedom pontoons. Energy 209, 118463. https://doi.org/10.1016/j.energy.2020.118463.

Ha, T., Lee, J.W., Cho, Y.S., 2011. Internal wave maker for Navier-Stokes equations in a three-dimensional numerical model. J. Coast Res. 511–515.

Hirt, C.W., Nichols, B.D., 1981. Volume of fluid (VOF) method for the dynamics of free boundaries. J. Comput. Phys. 39 (1), 201–225. https://doi.org/10.1016/0021-9991(81)90145-5.

Jakobsen, M.M., Beatty, S., Iglesias, G., Kramer, M.M., 2016. Characterization of loads on a hemispherical point absorber wave energy converter. International Journal of Marine Energy 13, 1–15. https://doi.org/10.1016/j.ijome.2016.01.003.

Kim, J., O'Sullivan, J., Read, A., 2012. Ringing analysis of a vertical cylinder by euler overlay method. Volume 4: offshore geotechnics, 855-866; Ronald W. Yeung Honoring Symposium on Offshore and Ship Hydrodynamics.

Kim, J., Tan, J.H.C., Magee, A., Wu, G., Paulson, S., Davies, B., 2013. Analysis of ringing response of a gravity based structure in extreme sea states. Proceedings of the ASME 2013 32nd International Conference on Ocean, Offshore and Arctic Engineering. Volume 7: CFD and VIV. Nantes, France. June 9–14, 2013. V007T08A077. ASME. https://doi.org/10.1115/OMAE2013-11466.

Kofoed, J.P., Frigaard, P., Friis-Madsen, E., Sørensen, H.C., 2006. Prototype testing of the wave energy converter wave dragon. Renew. Energy 31 (2), 181–189. https://doi.org/10.1016/j.renene.2005.09.005.

Konispoliatis, D.N., Mavrakos, S.A., 2020. Wave power absorption by arrays of wave energy converters in front of a vertical breakwater: a theoretical study. Energies 13 (8), 1985. https://doi.org/10.3390/en13081985.

Konispoliatis, D.N., Mavrakos, S.A., 2021. Hydrodynamic efficiency of a wave energy converter in front of an orthogonal breakwater. J. Mar. Sci. Eng. 9 (1), 94. https://doi.org/10.3390/jmse9010094.

Kramer, M., Marquis, L., Frigaard, P., 2011. Performance evaluation of the wavestar prototype. In: 9th Ewtec 2011: Proceedings of the 9th European Wave and Tidal Conference. Southampton, UK, 5th-9th September 2011.

Kraskowski, M., 2010. Simulating hull dynamics in waves using a RANSE code. Ship technology research = Schiffstechnik 57 (2), 120–127. https://doi.org/10.1179/str.2010.57.2.004.

Lal, A., Elangovan, M., 2008. CFD simulation and validation of flap type wave-maker. Int. J. Math. Comput. Sci. 2 (10), 708–714.

Le Méhauté, B., 2013. An Introduction to Hydrodynamics and Water Waves. Springer Science & Business Media.

Mavrakos, S.A., Katsaounis, G.M., Nielsen, K., Lemonis, G., 2004. Numerical performance investigation of an array of heaving wave power converters in front of a vertical breakwater. In: Proceedings of the International Offshore and Polar Engineering Conference.

McIver, P., Evans, D.V., 1988. An approximate theory for the performance of a number of wave-energy devices set into a reflecting wall. Appl. Ocean Res. 10 (2), 58–65. https://doi.org/10.1016/S0141-1187(88)80032-4.

Mustapa, M.A., Yaakob, O.B., Ahmed, Y.M., Rheem, C.-K., Koh, K.K., Adnan, F.A., 2017. Wave energy device and breakwater integration: a review. Renew. Sustain. Energy Rev. 77, 43–58. https://doi.org/10.1016/j.rser.2017.03.110.

Ning, D.-Z., Zhao, X.-L., Zhao, M., Hann, M., Kang, H.-G., 2017. Analytical investigation of hydrodynamic performance of a dual pontoon WEC-type breakwater. Appl. Ocean Res. 65, 102–111. https://doi.org/10.1016/j.apor.2017.03.012.

Ning, D., Zhao, X., Chen, L., Zhao, M., 2018. Hydrodynamic performance of an array of wave energy converters integrated with a pontoon-type breakwater. Energies 11 (3), 685. https://doi.org/10.3390/en11030685.

Ning, D., Zhao, X., Göteman, M., Kang, H., 2016. Hydrodynamic performance of a pile-restrained WEC-type floating breakwater: an experimental study. Renew. Energy 95, 531–541. https://doi.org/10.1016/j.renene.2016.04.057.

Paparella, F., Monk, K., Winands, V., Lopes, M.F.P., Conley, D., V.Ringwood, J., 2015. Up-wave and autoregressive methods for short-term wave forecasting for an oscillating water column. IEEE Trans. Sustain. Energy 6 (1), 171–178. https://doi.org/10.1109/tste.2014.2360751.

Pecher, A., Kofoed, J.P., 2017. Handbook of Ocean Wave Energy/. Springer Open, Cham, Switzerland *[internet resource]* (1st 2017.

Peric, R., Abdel-Maksoud, M., 2015. Assessment of Uncertainty Due to Wave Reflections in Experiments via Numerical Flow Simulations. The Twenty-fifth International Ocean and Polar Engineering Conference.

Perić, R., Abdel-Maksoud, M., 2016. Reliable damping of free-surface waves in numerical simulations. Ship Technol. Res. 63 (1), 1–13. https://doi.org/10.1080/09377255.2015.1119921.

Ransley, E.J., Greaves, D.M., Raby, A., Simmonds, D., Jakobsen, M.M., Kramer, M., 2017. RANS-VOF modelling of the Wavestar point absorber. Renew. Energy 109, 49–65. https://doi.org/10.1016/j.renene.2017.02.079.

Reabroy, R., Zheng, X., Zhang, L., Zang, J., Yuan, Z., Liu, M., Sun, K., Tiaple, Y., 2019. Hydrodynamic response and power efficiency analysis of heaving wave energy converter integrated with breakwater. Energy Convers. Manag. 195, 1174–1186. https://doi.org/10.1016/j.enconman.2019.05.088.

Richardson, L.F., 1911. IX. The approximate arithmetical solution by finite differences of physical problems involving differential equations, with an application to the stresses in a masonry dam. Philos. Trans. R. Soc. Lond. - Ser. A Contain. Pap. a Math. or Phys. Character 210 (459–470), 307–357. https://doi.org/10.1098/rsta.1911.0009.

Rodi, W., 1991. Experience with two-layer models combining the k-epsilon model with a one-equation model near the wall. In: 29th Aerospace Sciences Meeting. American Institute of Aeronautics and Astronautics. https://doi.org/10.2514/6.1991-216, 10.2514/6.1991-216.

Ruellan, M., BenAhmed, H., Multon, B., Josset, C., Babarit, A., Clement, A., 2010. Design methodology for a SEAREV wave energy converter. TEC 25 (3), 760–767. https://doi.org/10.1109/TEC.2010.2046808.

Schay, J., Bhattacharjee, J., Guedes Soares, C., 2013. Numerical Modelling of a Heaving Point Absorber in Front of a Vertical Wall, ume 8. Ocean Renewable Energy, 2013-06-09.

Tay, Z.Y., 2022a. Effect of resonance and wave reflection in semi-enclosed moonpool on performance enhancement of point absorber arrays. Ocean Eng. 243, 110182 https://doi.org/10.1016/j.oceaneng.2021.110182.

Tay, Z.Y., 2022b. Energy generation enhancement of arrays of point absorber wave energy converters via Moonpool's resonance effect. Renew. Energy 188, 830–848. https://doi.org/10.1016/j.renene.2022.02.060.

Tom, N., Ruehl, K., Ferri, F., 2018, 2018-06-17. Numerical Model Development and Validation for the WECCCOMP Control Competition, ume 10. Ocean Renewable Energy.

Tom, N.M., Madhi, F., Yeung, R.W., 2019. Power-to-load balancing for heaving asymmetric wave-energy converters with nonideal power take-off. Renew. Energy 131, 1208–1225. https://doi.org/10.1016/j.renene.2017.11.065.

Wang, Y., Wang, D., Dong, S., 2022. Theoretical study on arranging heaving wave energy converters in front of jarlan-type breakwater. Ocean Eng. 248, 110850 https://doi.org/10.1016/j.oceaneng.2022.110850.

Windt, C., Davidson, J., Ringwood, J.V., 2018. High-fidelity numerical modelling of ocean wave energy systems: a review of computational fluid dynamics-based numerical wave tanks. Renew. Sustain. Energy Rev. 93, 610–630. https://doi.org/10.1016/j.rser.2018.05.020.

Yemm, R., Pizer, D., Retzler, C., Henderson, R., 2012. Pelamis: experience from concept to connection. Proc. R. Soc. A 370 (1959), 365–380. https://doi.org/10.1098/rsta.2011.0312.

Zhang, H., Ding, X., Zhou, B., Zhang, L., Yuan, Z., 2019. Hydrodynamic performance study of wave energy–type floating breakwaters. J. Mar. Sci. Appl. 18 (1), 64–71. https://doi.org/10.1007/s11804-019-00064-y.

Zhao, X., Zhang, Y., Li, M., Johanning, L., 2020. Hydrodynamic performance of a Comb-Type Breakwater-WEC system: an analytical study. Renew. Energy 159, 33–49. https://doi.org/10.1016/j.renene.2020.05.100.

Zhao, X., Zhang, Y., Li, M., Johanning, L., 2021. Experimental and analytical investigation on hydrodynamic performance of the comb-type breakwater-wave energy converter system with a flange. Renew. Energy 172, 392–407. https://doi.org/10.1016/j.renene.2021.02.138.

Zhao, X.L., Ning, D.Z., Liang, D.F., 2019a. Experimental investigation on hydrodynamic performance of a breakwater-integrated WEC system. Ocean Eng. 171, 25–32. https://doi.org/10.1016/j.oceaneng.2018.10.036.

Zhao, X.L., Ning, D.Z., Zou, Q.P., Qiao, D.S., Cai, S.Q., 2019b. Hybrid floating breakwater-WEC system: a review. Ocean Eng. 186, 106126 https://doi.org/10.1016/j.oceaneng.2019.106126.